NUMERICAL MODEL DEVELOPED FOR THERMO-MECAHNICAL ANALYSIS IN AlCrFeMnNiHf$_{0.05}$–ARMOX 500 STEEL WELDED JOINT

D. C. Birsan[1], G. Simion[1*], I. Voiculescu[2], E. Scutelnicu[1]

[1] "Dunarea de Jos" University of Galati, Faculty of Engineering, Romania
[2] Polytechnic University of Bucharest, Department of Materials Technology and Welding, Romania
*Corresponding author's e-mail address: george.simion@ugal.ro

ABSTRACT

High entropy alloys are a new category of materials that contain at least four main chemical elements. One of the main advantages over the traditional alloys is the ability to maintain their properties at low or high temperatures. Researchers have investigated the possibility of welding these alloys so that they can be used in industrial applications. Good results have been obtained by welding butt joints of thin sheets, without the use of filler materials. In this paper it is investigated the possibility of welding overlap joints, with applications in the military field, of medium-thickness plates of AlCrFeMnNiHf$_{0.05}$ high entropy alloy on an Armox 500 steel support plate, using filler materials available on the market. The research focuses on the numerical simulation of three welding processes commonly used in on-site repair operations, namely manual metal arc, metal inert gas, and tungsten inert gas.

KEYWORDS: high entropy alloy, steel, welding, numerical simulation.

1. INTRODUCTION

High Entropy Alloys (HEAs) are a new category of materials that has attracted the attention of researchers in the last two decades [1]-[5]. When first developed, Yeh and others defined them as alloys composed of at least 5 main chemical elements in equiatomic or approximately equiatomic concentrations without a dominant chemical element [6], [7]. Over time, however, with the increase in the number of experiments performed, it has been accepted that these alloys may have at least four main chemical elements [8]-[11], with an atomic ratio ranging from 5% to 35%. Although there are some HEAs that have remarkable mechanical properties [12]-[14], the main advantage of these materials that makes them suitable for replacing traditional alloys is their ability to maintain their properties at cryogenic temperatures [15], [16] or high ones [17]-[19].

Welding is one of the most used technology in manufacturing processes. Therefore, the researchers considered it necessary to investigate the weldability of HEAs in order to use them in industrial applications [20]-[22]. Thus, Zhu Z. G. et al. in [23] studied the behavior of CoCrFeNi alloy using friction stir welding (FSW). Another material studied is the CoCrFeMnNi alloy, welded using the electron beam welding process in [24] by Wu Z. et al., Tungsten Inert Gas (TIG) welding process by Wu Z. et al in [25], laser welding process by Kashaev N. et al. [26] and Nam et al. [27] and by the FSW welding process by Jo M. G. et al. [28] and Shaysultanov D. et al. [29]. The AlCoCrCuFeNi alloy has been successfully welded by Martin A. et al. using laser and TIG welding processes [30]. The AlCrFeCoNi alloy has been welded by Sokkalingam R. et al. using laser and TIG welding processes [31],32], by Nahmany M. et al. using the electron beam welding process [33] and by Zhu Z.G. et al. using the FSW welding process [34]. Studies performed so far on the weldability of high entropy alloys obtained good results but they focused on butt welding of thin sheets without the use of filler metal. In this paper it is investigated the possibility of overlap welding medium thickness plates of dissimilar materials (AlCrFeMnNiHf$_{0.05}$ alloy and ARMOX 500 steel), using filler materials available on the market, with applicability in the manufacture of ballistic protection systems in the military field.

2. MATERIALS AND METHODS

In this paper it is investigated the possibility of lap welding a 60x60x6mm AlCrFeMnNiHf$_{0.05}$ HEA plate on a 120x120x12mm ARMOX 500 steel plate, (Fig. 1). Three commonly used welding processes on in situ intervention [35] are considered: Manual Metal Arc (MMA), Metal Inert Gas (MIG), and Tungsten Inert Gas.

The MRF ABJ 900 vacuum spring melting installation within the ERAMET - SIM - UPB

Date of submission/acceptance: 02.09.2021/15.12.2021 https://doi.org/10.35219/awet.2021.05

Laboratory has been used to obtain the HEA ingots. Advanced purity metallic materials have been selected according to the chemical composition and particle size analysis, in order to be well-positioned in the water-cooled copper plate of the installation's mold. The chemical compositions of the metallic materials used for the production of AlCrFeMnNi, HEA system microalloyed with Hf are as follows: mild steel, mark MK3: Si = 0.04%; C = 0, 02%; S = 0.02%; Mn = 0.21%; Ni = 0.2%,P = 0.015%; Cr = 0.15%; Cu = 0.14%; Mo = 0.07%; Al = 0.12%; Fe = balance%, metallic chromium with 99% Cr, electrolytic aluminum with 98.5% Al, metallic manganese with 99.9% Mn, electrolytic nickel with 99.5% Ni, Hafnium metal granules of 99.5% purity.

The metallic materials have been mechanically prepared by cutting to convenient sizes and chemically pickled to remove eventually oxides. To ensure a high homogeneity of the alloys, the load has been remelted 6 times.

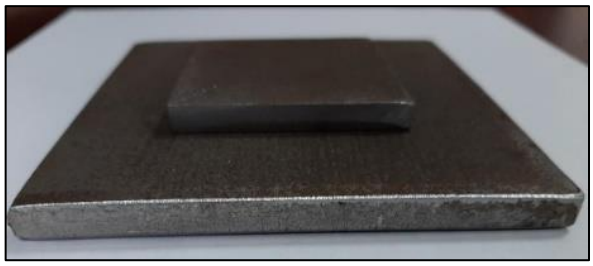

Fig. 1. Samples prepared for welding

The metallographic analysis has been performed using an Olympus GX 51 inverted optical microscope, and it could be observed a partially dissolved Hf particle (Fig. 2. a), imperfection caused by the high melting temperature of this material (2150°C.), the dendritic microstructure of the alloy (Fig.2.b) and uniformly dispersed compounds (yellow color) (Fig. 2.c).

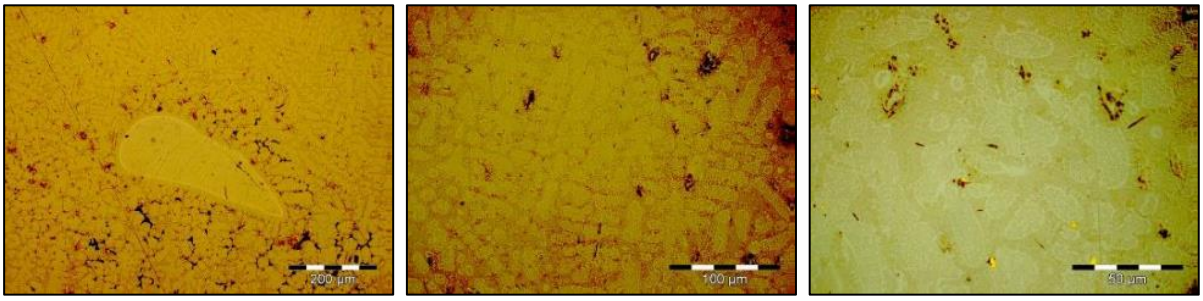

a) b) c)

Fig. 2. Metallographic analysis of $AlCrFeMnNiHf_{0.05}$ alloy

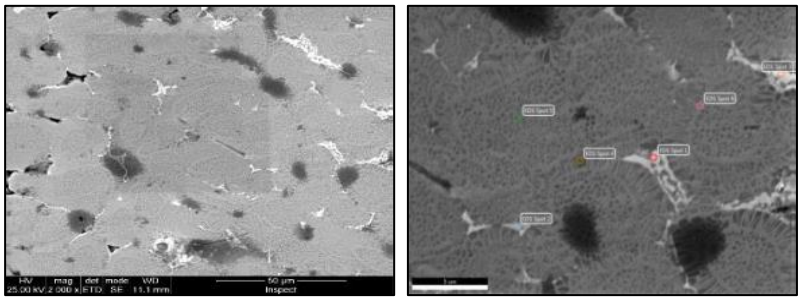

Element	Weight%	Atomic%
Al	10.47	19.65
Cr	20.15	19.63
Mn	21.63	19.94
Fe	21.36	19.34
Ni	22.9	20.45
Hf	3.49	0.99

a) b) c)

Fig. 3. SEM analysis of $AlCrFeMnNiHf_{0.05}$ alloy

SEM analysis (Fig. 3) has been performed in different zones using an FEI electron microscope, equipped with an EdAX Apex 2Ze analyser, and the medium chemical composition of the HEA is presented in figure 3.c.

$AlCrFeMnNiHf_{0.05}$ plates have been lap welded to the support ARMOX 500 steel plate by the following welding processes: MMA, MIG, and TIG using STARINOX 316L as filler material. The mechanical characteristic and chemical composition of the materials are presented in tables 1 and 2. The three welding processes were performed in two passes and the following main parameters have been applied:

- MMA: 120A current, 20V voltage, 12cm/min welding speed;
- MIG: 140A current, 24V voltage, 14cm/min welding speed;
- TIG: 180A current, 17V voltage, 10cm/min welding speed.

Table 1. Chemical composition of the base materials and filler metal

Material	C	Si	Mn	P	S	Cr	Ni	Mo	B	Fe	Al	Hf
ARMOX 500	0.32	0.4	1.2	0.01	0.003	1	1.8	0.7	0.005	96.96	-	-
STARINOX 316L	0.035	0.8	0.9	0.025	0.025	19	12	2.6	-	61.615	-	-
$AlCrFeMnNiHf_{0.05}$	-	-	21.63	-	-	20.15	22.9	-	-	21.63	10.47	3.49

Table 2. Mechanical properties of the base materials and filler metal

Material	Hardness	Yield Strength Rp0.2 min [MPa]	Tensile Strength Rm [MPa]	Elongation min [%]
ARMOX 500	480-540 [HBW]	1250	1450-1745	10
STARINOX 316L	-	350	510	30
$AlCrFeMnNiHf_{0.05}$	460-490 [HV0.2]	1220	1610	10

3. NUMERICAL MODELLING

A semi-ellipsoidal source has been considered in order to simulate the welding of the AlCrFeMnNi0.05Hf plate on the ARMOX 500 one, for all of the three processes studied (MMA, MIG, and TIG). Simufact Welding is the software used to conduct the simulation and the considered finite element model is presented in figure 4.

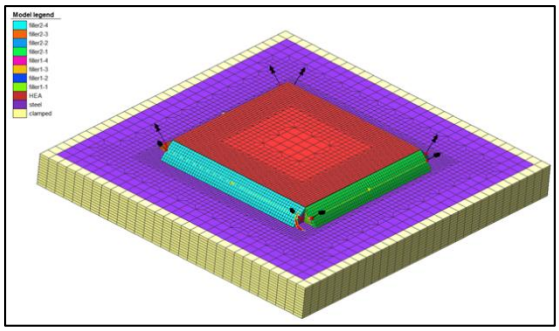

Fig. 4. 3D Global finite element model

SOLID7, a parallelepiped three-dimensional, isoparametric finite element with eight nodes, has been used, recommended for a thermo-structural analysis. The values of temperature and the heat flux gradient have been analyzed in all regions of the welded joint. Particular attention, from the point of view of the refinement of the discretization mesh, has been given to the heat affected zone, due to the fact that the most important changes of the stresses caused by the welding process occur in this area. The three-dimensional model considered consists of 99000 elements, 73800 for the steel plate and 25200 for the HEA plate. The elements of the weld beads are deactivated at the beginning of the simulation process and are activated when the heat source passes through them, in order to simulate the deposition of molten metal. In the developed numerical models, the weld bead and the base materials have been considered three different bodies, in direct contact, shown in figure 4.

To simulate the welding processes and minimize the errors of the numerical models, the input data (welding parameters and dimensions of the molten metal pool) have been collected from the experimental program. The thermal flux is semi-ellipsoid volumetric, according to the model of Goldak's thermal source [36]. The model of the heat source is presented in figure 5, where a_f is front length, a_r - rear length, b - width, d – depth. The values for these dimensions as well as the heat input of the welding processes are presented in table 3

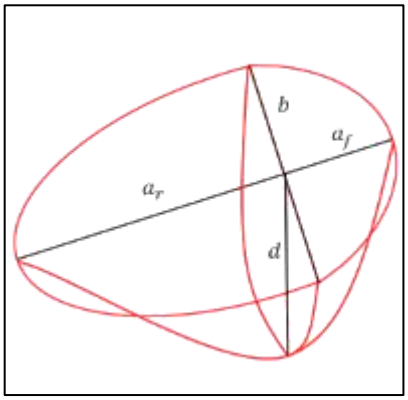

Fig. 5. Heat source model

Table 3. Dimensions of heat sources and heat input

Welding process	Dimensions of heat sources [mm]		Heat Input [kJ/mm]
MMA	a_f	1.2	0.84
	a_r	6.0	
	b	4.0	
	d	4.0	
MIG	a_f	2.0	1.15
	a_r	9.5	
	b	5.0	
	d	5.0	
TIG	a_f	2.0	1.1
	a_r	10.0	
	b	5.0	
	d	5.2	

In numerical modeling of the welding processes, the following assumptions have been considered:

- isotropy of the base material
- variation of thermo-physical-mechanical properties depending on temperature;
- heat loss to the environment through convection and radiation;
- heat transfer coefficient at the contact interface between the work pieces and the air: 12W/m^2/°C;
- T_{melt_HEA} = 1463ºC and T_{melt_steel} = 1528°C;
- ambient temperature: 20°C;
- heat transfer propagates in all three directions;
- movement of the metal in the welding pool is neglected.

The AlCrFeMnNiHf$_{0.05}$ alloy has been defined and introduced into the finite element analysis program based on the analysis of chemical elements provided from the experimental determinations as can be seen in figure 6.

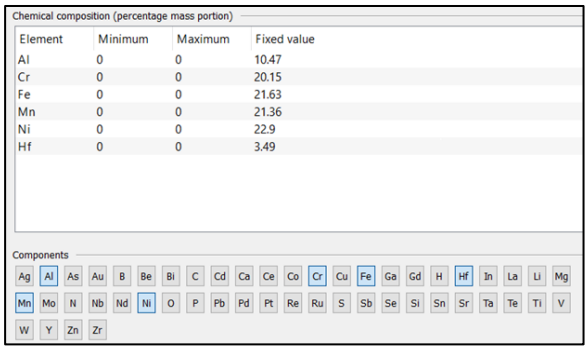

Fig. 6. Chemical composition of AlCrFeMnNiHf$_{0.05}$

4. RESULTS AND DISCUSSION

Numerical modelling and simulation focused on the analysis of the thermal field and the residual stresses that appear in the welded joint.

4.1. Thermal Field Analysis

Knowing the melting temperature of the materials from which the two components are manufactured, (T_{melt_HEA} = 1463°C, and T_{melt_steel} = 1528°C), it is possible to estimate the maximum size of the molten weld pool, in the quasi-stationary phase of the welding process. In figure 7 it is presented the thermal field distribution generated by the heat source of the welding processes during the second pass. The maximum temperature reached in the weld pool is around 1950°C on the first pass and 2100°C on the second one. The analysis of the thermal field allows the estimation of the HAZ dimensions in the welded joint. The welding process is unstable at the beginning and in the transient phase due to the low temperature of the plates, therefore the heat affected zone is slightly extended. In the quasi-stationary phase, the welding process is stabilized, and the shape of the thermal field, induced by the welding process, is constant. In the case of the MMA process during the first pass, the width of the HAZ reaches values of approximately 3.9mm in the AlCrFeMnNiHf$_{0.05}$ plate and 3.3mm in ARMOX 500 one as can be seen in table 4. HAZ size is influenced by the thermal diffusivity of the material, low thermal diffusivity determining an extended HAZ. Thus, taking into consideration the fact that the AlCrFeMnNiHf$_{0.05}$ HEA plate has a lower thickness and a higher thermal diffusivity, it is difficult to determine which characteristic generated a more extended HAZ in this plate.

During the second pass, it is observed an extension of the HAZ, due to the fact that the components are already preheated by the first pass, its values reaching approximately 5.5mm in AlCrFeMnNiHf$_{0.05}$ and 4.2mm in ARMOX 500 for the MMA process. As expected, from all the three process analyzed, TIG welding generates the largest heat affected zone due to the high heat input and low welding speed that are specific to this process. The approximate dimensions of the HAZ for the MMA, MIG, and TIG welding process for the first and second pass are presented in table 4. It is also noted that the shape and size of the weld pool are also influenced by the preheated state on the components, being larger in the second pass even though the welding parameters are identical in both passes.

Table 4. Heat affected zone dimensions

Welding process	Material	HAZ dimension - first pass [mm]	HAZ dimension - second pass [mm]
MMA	AlCrFeMnNiHf$_{0.05}$	3.9	5.5
	ARMOX 500	3.3	4.2
MIG	AlCrFeMnNiHf$_{0.05}$	6.3	12.5
	ARMOX 500	4.8	10
WIG	AlCrFeMnNiHf$_{0.05}$	6.7	14.8
	ARMOX 500	5.3	12

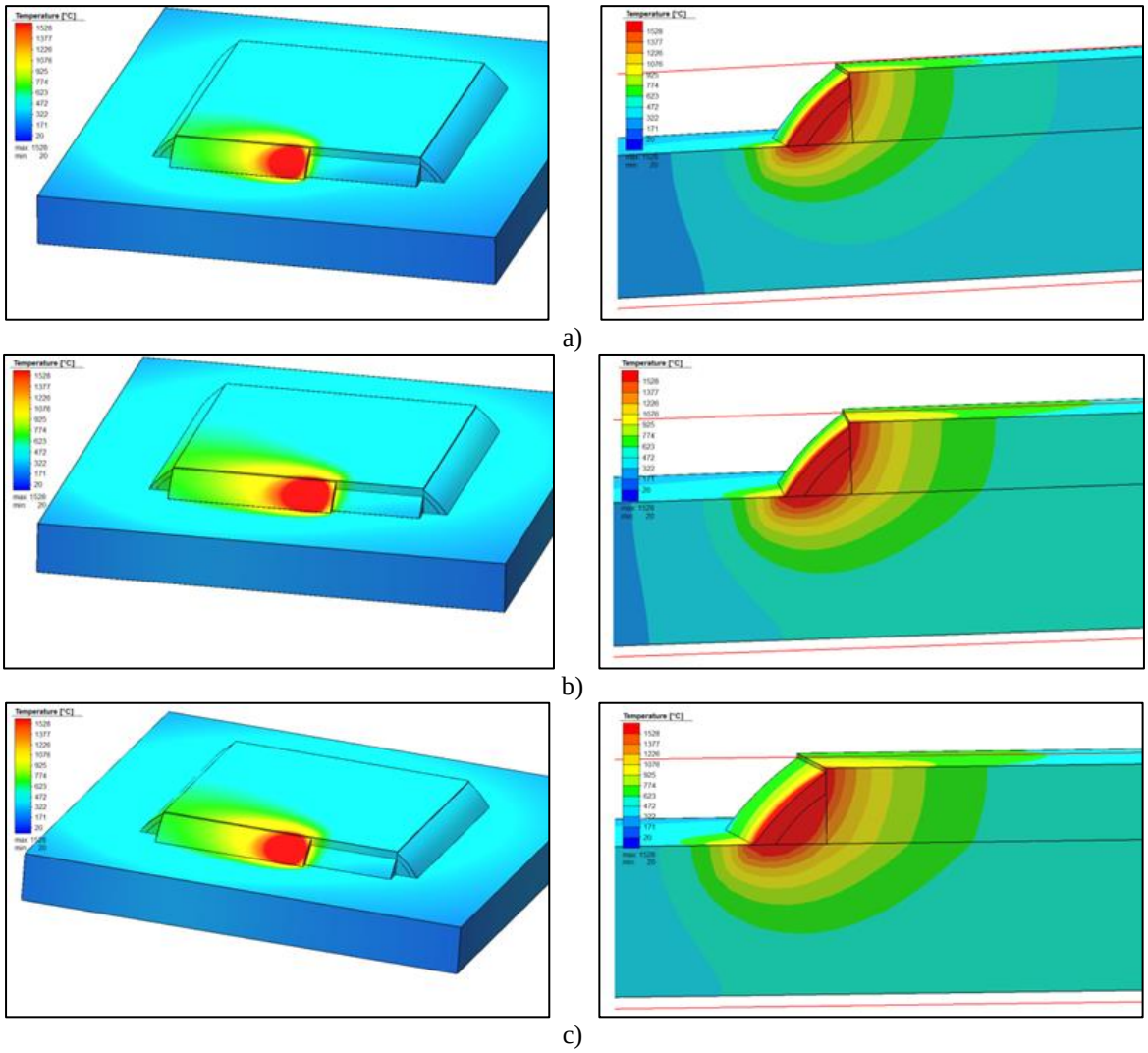

Fig. 7. Thermal field - the second pass (a) MMA, (b) MIG, (c) TIG

In order to perform the analyses on the thermal cycles and Von Mises stress, nodes were positioned from millimeter to millimeter on the surface of the components, arranged transversely to the direction of the welding bead (Fig. 8).

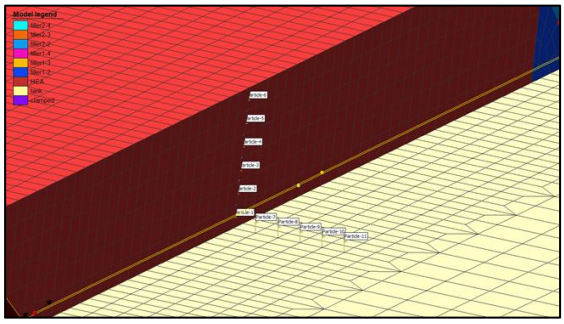

Fig. 8. The position of the nodes in which the thermal cycles have been analyzed

From of thermal cycles' graphs (Fig. 9), it can be observed that, for the first pass, in the case of MMA welding, the maximum temperature is recorded near node 4 in the $AlCrFeMnNiHf_{0.05}$ plate (approximately 1700°C and near node 9 in the ARMOX 500 plate (approximately 1750°C), sixteen seconds from the beginning of the welding process when the weld pool reaches this area. At the second pass, the maximum temperatures are reached in nodes 5 ($AlCrFeMnNiHf_{0.05}$ plate) and 10 (ARMOX 500 plate) and are approximately 3% (50°C) higher than the ones registered in the first pass, due to the interpass temperature. For the other two analyzed welding processes (MIG / TIG) it is found that the same trends are maintained - higher temperatures in the ARMOX 500 plate than in the $AlCrFeMnNiHf_{0.05}$ one, and an increase of these values during the second pass. The increased heat input used by these processes generates higher temperatures, the peak values reaching around 1900°C for the MIG welding process and 2000°C for the TIG welding process. As in the case of the heat affected zone, the temperature difference between the two materials is influenced by the thermal diffusivity and heat dissipation.

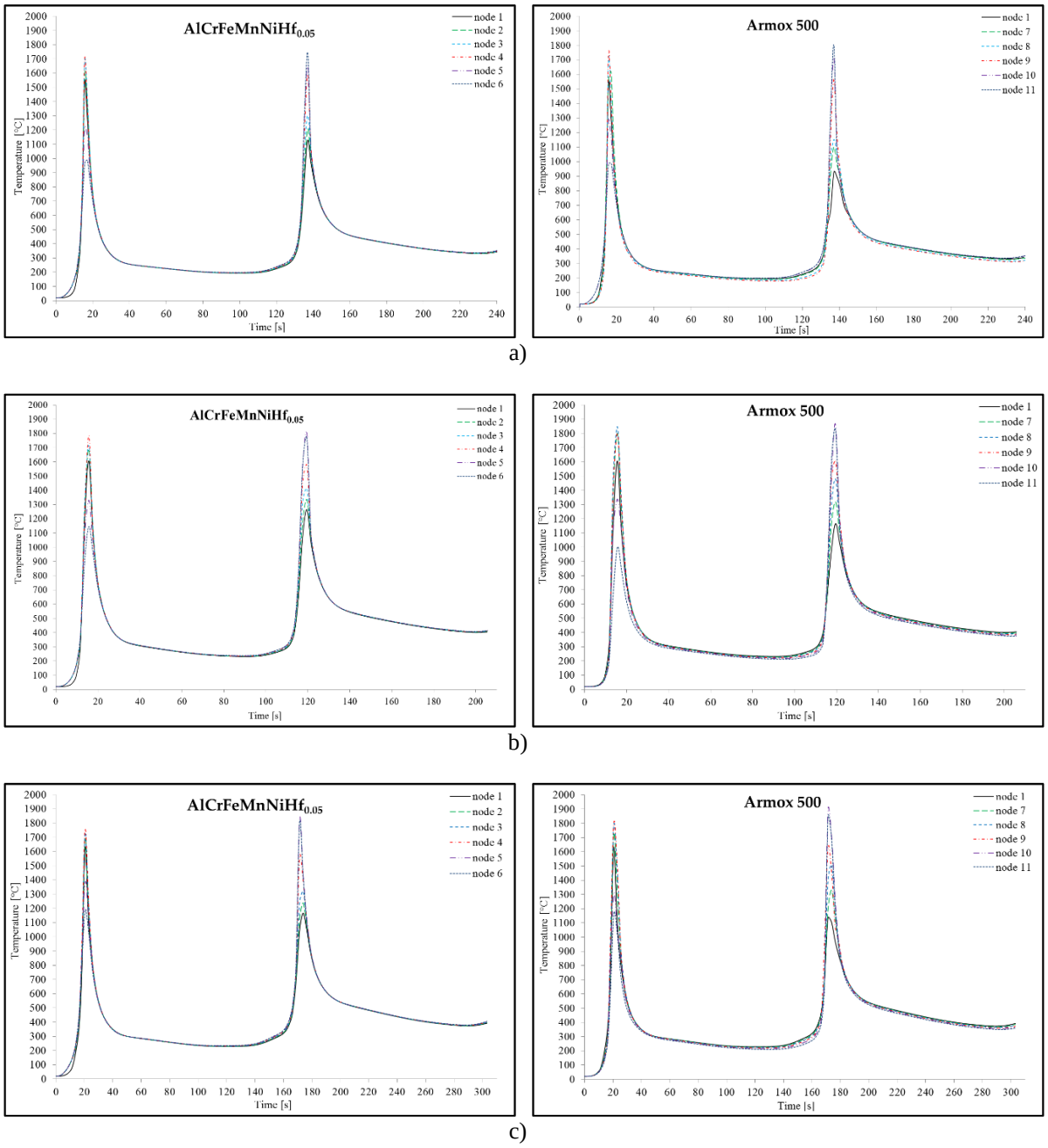

Fig. 9. Thermal cycles in the considered nodes: a) MMAW; b) MIG; c) TIG

4.2. Von Mises Stresses

During the welding process, the stresses generated by the expansion of the components produced during the heating phase are distributed unevenly and their value decreases with the distance from the fusion line. When the weld pool solidifies, contraction stresses appear in the weld area. Due to the fact that the expansions and contractions of the metal do not occur uniformly, internal stresses develop which, if they exceed the critical values, lead to the appearance of deformations or cracks. Therefore, in the welded joint there will be high temperature areas and cold ones that will influence each other, the colder areas opposing both the expansion and the contraction of the material caused by heating and cooling. A consequence of those described is the appearance of thermal, mechanical, and structural stresses in the welded joint, leading to tension and deformation. In figure 10 it is presented the global distributions of stress in the joint during the second pass, it can be seen that the corners of the $AlCrFeMnNiHf_{0.05}$ plate are stress concentrators. As expected, TIG welding process generates the highest values of Von Mises stress due to its high heat input and low welding speed.

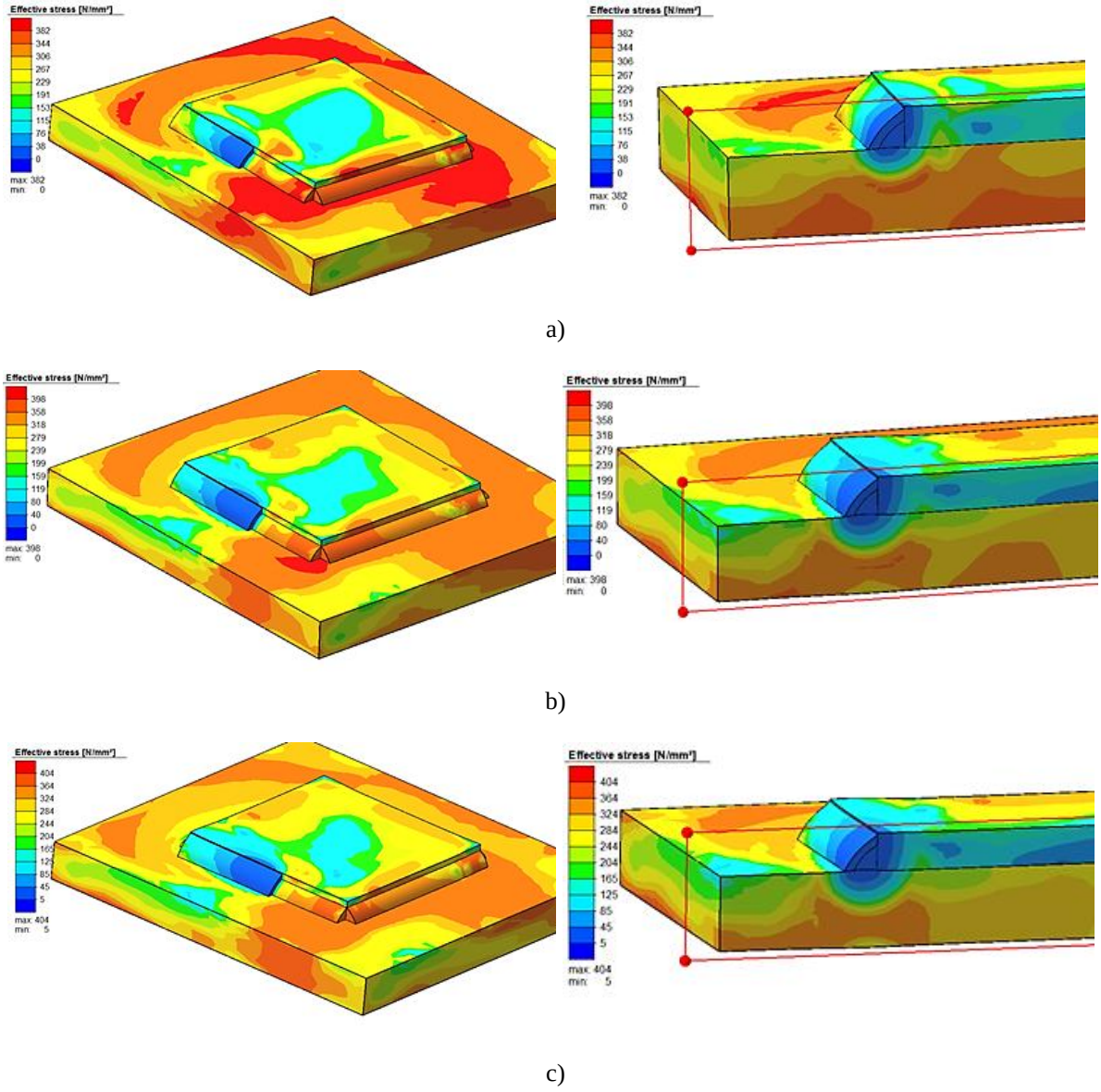

Fig. 10. Effective stresses map: a) MMAW; b) MIG; c) TIG

Figure 11 presents a time variation of the Von Mises stress in the nodes considered in figure 7. It is observed that the Von Mises stresses have a sudden increase in values when the heat source approaches the analyzed area due to the expansion stresses that occur.

The tensile values then drop close to zero when the weld pool reaches this zone. The stresses then increase abruptly after about 15 seconds from the start of the solidification process and are maintained on a level that has a slightly increasing tendency correlating with a decrease in temperature. The peak value of stresses (384MPa in the $AlCrFeMnNiHf_{0.05}$ plate and 398MPa in the ARMOX 500 steel plate) corresponds to the minimum value of temperature in this area.

The value of the stresses starts to decrease with the increase of the temperature due to the approach of the heat source. After the second pass, the maximum values of the Von Mises stress reach values of 346MPa for $AlCrFeMnNiHf_{0.05}$ plate and 363MPa for ARMOX 500 steel plate. The decrease of the peak values of the stress by approximately 9-10% as well as the stress decreasing tendency after the second pass are attributed to the beneficial effects of the interpass temperature. The same tendency of stress development is also found in the case of the other two welding processes analyzed (MIG and TIG), the values being higher due to the greater heat input used.

The maximum values of the Von Mises stress in the considered nodes for the three processes are presented in table 5.

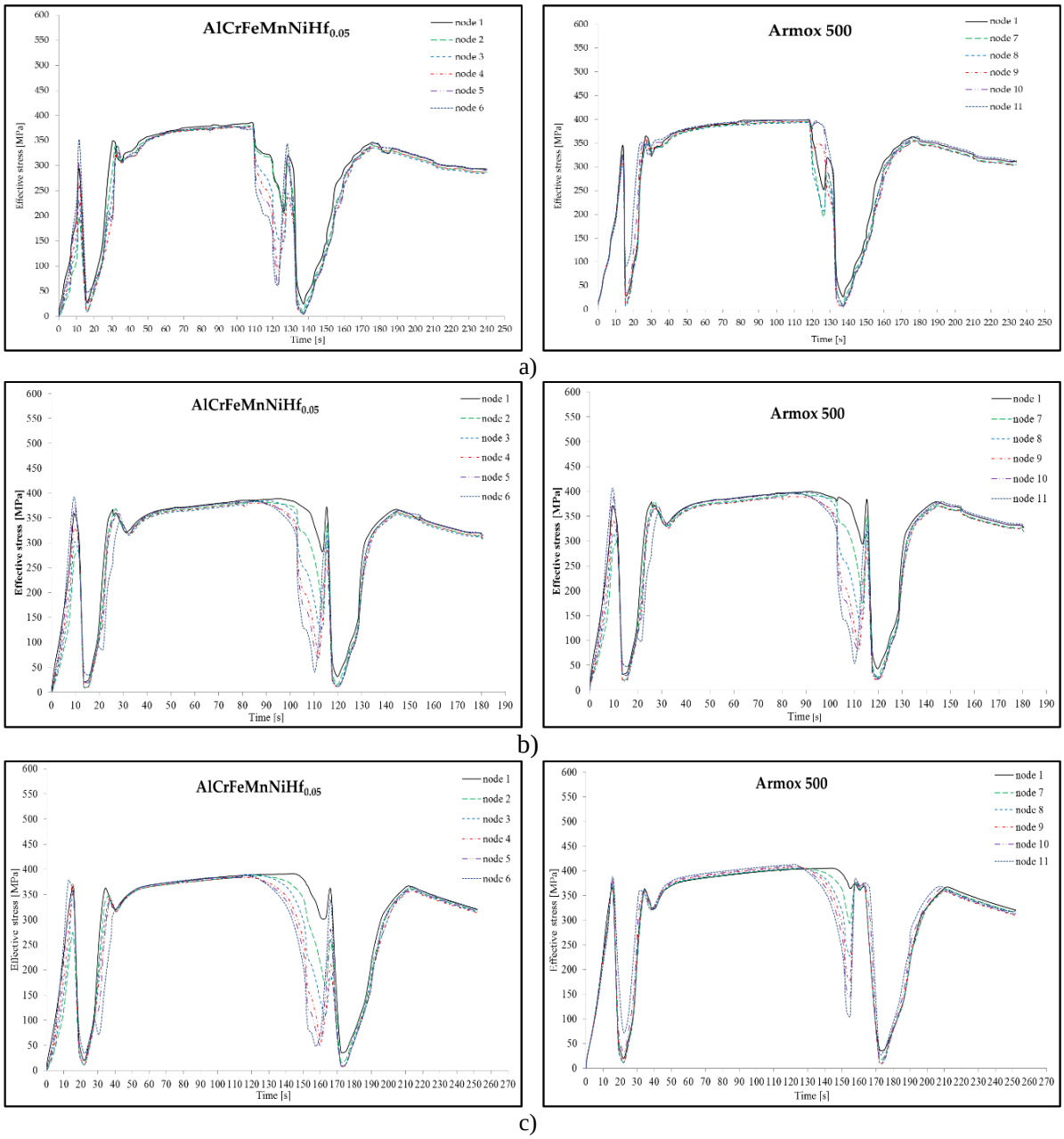

Fig. 11. Effective stresses in the considered nodes (a) MMAW, (b) MIG, (c) TIG

Table 5. Von Mises stress peak values in considered nodes

Welding process	Material	Von Mises stress after first pass [MPa]	Von Mises stress after second pass [MPa]
MMA	$AlCrFeMnNiHf_{0.05}$	384	346
	ARMOX 500	398	363
MIG	$AlCrFeMnNiHf_{0.05}$	392	367
	ARMOX 500	406	379
TIG	$AlCrFeMnNiHf_{0.05}$	391	366
	ARMOX 500	412	368

5. CONCLUSIONS

Based on the research carried out in the paper, the following conclusions can be drawn:

- In the welded joint it is observed the development of a more extensive thermally affected area in the $AlCrFeMnNiHf_{0.05}$ plate than on the ARMOX 500 one, but taking into account the fact that the $AlCrFeMnNiHf_{0.05}$ plate has a lower thickness and a higher thermal diffusivity, it cannot be precise to determine which characteristic generated a more extended HAZ in this plate.
- The analysis of the thermal fields demonstrated that the higher temperatures are reached in the ARMOX 500 plate and that the interpass temperature leads to the increase of the maximum temperatures during the second pass.
- Von Mises stresses reach higher values in the ARMOX 500 plate and it can be observed that there is a decrease in them after the second pass due to the presence of the interpass temperature.
- Among the welding processes analyzed TIG was the one who generated the highest values for the for the peak temperatures and Von Mises stresses, and the most extended HAZ due to the high energy input and slow welding speed that are characteristic of this process.

In the following research it will be investigated the possibility of welding other high entropy alloys using filler materials that are currently available on the market; as well as identifying the optimal technical solutions to reduce stresses and strains that occur in welded joints.

REFERENCES

[1] **Ye Y. F., Wang Q., Lu J., Liu C. T., Yang Y.,** *High-entropy alloy: challenges and prospects*, Materials Today, Volume 19, Number 6, July/August 2016, pp. 349-362.

[2] **Miracle D. B., Senkov O. N.,** *A critical review of high entropy alloys and related concepts*, Acta Materialia, Vol. 122, 2017, pp. 448-511.

[3] **Lu Z. P., Wang H., Chen M. W., Baker I., Yeh J. W., Liu C. T., Nieh T. G.,** *An assessment on the future development of high-entropy alloys: summary from a recent workshop*, Intermetallics, Vol. 66, 2015, pp. 67–76.

[4] **Moravcik I., Kubicek A., Moravcikova-Gouvea L., Adam O., Kana V., Pouchly V., Zadera A., Dlouhy I.,** *The Origins of High-Entropy Alloy Contamination Induced by Mechanical Alloying and Sintering*, Metals **2020**.

[5] **Cui W., Li W., Chen W. T., Liou F.,** *Laser Metal Deposition of an AlCoCrFeNiTi0.5 High-Entropy Alloy Coating on a Ti6Al4V Substrate: Microstructure and Oxidation Behavior*, Crystals, 2020.

[6] **Murty B. S., Yeh J. W., Ranganathan S.,** *High-Entropy Alloys*, Elsevier Inc., 2014**.**

[7] **Yeh J. W., Chen Y.L, Lin S. J., Chen S. K.,** *HIGH-ENTROPY ALLOYS – A New Era of Exploitation*, Materials Science Forum Vol. 560, 2007, pp. 1-9.

[8] **Shao Y., Ma H., Wang Y.,** *Effect of Mo Addition on The Microstructure and Mechanical Properties of CoCuFeNi High Entropy Alloy*, Metals 2020, 10, 1017.

[9] **Wu Z., Bei H., Otto F., Pharr G. M., George E. P.,** *Recovery, recrystallization, grain growth and phase stability of a family of FCC-structured multi-component equiatomic solid solution alloys*, Intermetallics 46, 2014, pp.131-140.

[10] **Lee C., Chou Y., Kim G., Gao M.C., An K., Brechtl J., Zhang C., Chen W., Poplawsky J.D., Song G., Ren Y., Chou Y.C., Liaw P.K**.*, Lattice-Distortion-Enhanced Yield Strength in a Refractory High-Entropy Alloy*, Advanced Materials, 2020, 32.

[11] **Lindner T., Löbel M., Saborowski, E., Rymer L.M., Lampke T.,** *Wear and Corrosion Behaviour of Supersaturated Surface Layers in the High-Entropy Alloy Systems CrMnFeCoNi and CrFeCoNi*, Crystals, 2020.

[12] **Youssef K. M., Zaddach A. J., Niu C., Irving D. L., Koch C. C.,** *A Novel Low-Density, High-Hardness, High-entropy Alloy with Close-packed Single-phase Nanocrystalline Structures*, Materials Research Letters, Vol. 3, 2015, pp. 95-99.

[13] **Moon J., Qi Y., Tabachnikova E., Estrin Y., Choi W.M., Joo S.H., Lee B.J., Podolskiy A., Tikhonovsky M., Kim H.S.,** *Microstructure and Mechanical Properties of High-Entropy Alloy Co20Cr26Fe20Mn20Ni14 Processed by High-Pressure Torsion at 77K and 300K*, Scientific Reports, 2018, 8:11074.

[14] **Larianovsky N., Demyanetz A.K., Eshed E., Regev M.,** *Microstructure, Tensile and Creep Properties of Ta20Nb20Hf20Zr20Ti20 High Entropy Alloy*, Materials, 2017.

[15] **Liu J., Guo X., Lin Q., He Z., An X., Li L., Liaw P. K., Liao X., Yu L., Lin J., Xie L., Ren J., Zhang Y.,** *Excellent ductility and serration feature of metastable CoCrFeNi high-entropy alloy at extremely low temperatures*, SCIENCE CHINA Materials, 2018.

[16] **Zherebtsov S., Stepanov N., Ivanisenko Y., Shaysultanov D., Yurchenko N., Klimova M., Salishchev G.,** *Evolution of Microstructure and Mechanical Properties of a CoCrFeMnNi High-Entropy Alloy during High-Pressure Torsion at Room and Cryogenic Temperatures*, Metals, 2018.

[17] **Waseem O.A., Ryu H.J.,** *Combinatorial development of the low-density high-entropy alloy Al10Cr20Mo20Nb20Ti20Zr10 having gigapascal strength at 1000 °C*, Journal of Alloys and Compounds, Vol. 845, 2020**.**

[18] **Wang W. R., Wang W. L., Yeh J. W.,** *Phases, microstructure and mechanical properties of AlxCoCrFeNi high-entropy alloys at elevated temperatures*, Journal of Alloys and Compounds, Vol. 589, 2014, pp. 143-152.

[19] **Voiculescu I., Geantă V., Stefănoiu R., Rotariu A., Scutelnicu E., Pantilimon M.C., Mitrică D., Crăciun V**., *New refractory high entropy alloys*, IOP Conference Series: Materials Science and Engineering, 572, 2019, 012024

[20] **Lopes J. G., Oliveira J. P.,** *A Short Review on Welding and Joining of High Entropy Alloys*. Metals, 2020.

[21] **Guo J., Tang C., Rothwell G., Li L., Wang Y. C., Yang Q., Ren X.,** *Welding of High Entropy Alloys—A Review*, Entropy, 2019.

[22] **Scutelnicu E., Simion G., Rusu C.C., Gheonea M.C., Voiculescu I., Geanta V.,** *High Entropy alloys during welding*, Revista de chimie, Vol 71, Issue 3, pp. 219-233.

[23] **Zhu Z.G., Sun Y. F., Ng F.L., Goh M. H., Liaw P. K., Fujii H., Nguyen Q. B., Xu Y., Shek C. H., Nai S. M. L., Wei J.,** *Friction-stir welding of a ductile high entropy alloy: microstructural evolution and weld strength*, Materials Science & Engineering A, Vol. 711, 2018, pp. 524-532.

[24] **Wu Z., David S.A., Leonard D.N., Feng Z., Bei H.,** *Microstructures and mechanical properties of a welded CoCrFeMnNi high-entropy alloy*, Science and Technology of Welding & Joining, 2018, Vol. 23, pp. 585-595.

[25] **Wu Z., David S.A., Feng Z., Bei H.,** *Weldability of a high entropy CrMnFeCoNi alloy*, Scripta Materiala, Vol. 124, 2016, pp. 81-85.

[26] **Kashaev N., Ventzke V., Stepanov N., Shaysultanov D., Sanin V., Zherebtsov S.,** *Laser beam weldingof a CoCrFeNiMn-type high entropy alloy produced by self-propagating high-temperature synthesis*, Intermetallics, Vol. 96, **2018**, pp. 63-71.

[27] **Nam H., Parka C., Moon J., Na Y., Kim H., Kang N.,** *Laser weldability of cast and rolled high-entropy alloys for cryogenic applications*, Materials Science & Engineering A, Vol. 742, 2019, pp. 224-230.

[28] **Jo M. G., Kim H. J., Kang M., Madakashira P. P., Park E. S., Suh J. Y., Kim D. I., Hong S. T., Ha N. H.,** *Microstructure and Mechanical Properties of Friction Stir Welded and Laser Welded High Entropy Alloy CrMnFeCoNi*, Metals and Materials International, Vol. 24, nr. 1, 2018, pp. 73-83.

[29] **Shaysultanov D., Stepanov N., Malopheyev S., Vysotskiy I., Sanin V., Mironov S., Kaibyshev R., Salishchev G., Zherebtsov S.,** *Friction stir welding of a carbon-doped CoCrFeNiMn high-entropy alloy*, Materials Characterization, 2018.
[30] **Martin A. C., Fink C.,** *Initial weldability study on Al0.5CrCoCu0.1FeNi high-entropy alloy*, Welding in the World, Vol. 63, 2019, pp. 739–750.
[31] **Sokkalingam R., Mishra S., Cheethirala S.R., Muthupandi V., Sivaprasad K.,** *Enhanced Relative Slip Distance in Gas-Tungsten-Arc-Welded Al0.5CoCrFeNi High-Entropy Alloy*, Metallurgical and Materials Transactions, Vol. 48, 2017, pp. 3630-3634.
[32] **Sokkalingam R., Sivaprasad K., Muthupandi V., Duraiselvam M.,** *Characterization of Laser Beam Welded Al0.5CoCrFeNi High-Entropy Alloy*, Key Engineering Materials, Vol. 775, 2018, pp. 448–453.
[33] **Nahmany M., Hooper Z., Stern A., Geanta V., Voiculescu I.,** *AlxCrFeCoNi High-Entropy Alloys: Surface Modification by Electron Beam Bead-on-Plate Melting*, Metallography Microstructure and Analysis, Vol. 5, 2016, pp. 229-240.
[34] **Zhu Z. G., Sun Y. F., Goh M. H., Ng F. L., Nguyen Q. B., Fujii H., Nai S. M. L., Wei J., Shek C.H.,** *Friction stir welding of a CoCrFeNiAl0.3 high entropy alloy*, Materials Letters, Vol. 205, 2017, pp. 142-144.
[35] **Gheonea M.C., Mihăilescu D., Florescu S.N., Scutelnicu E.**, *Experimental research on melting and deposition characteristics of wires during gas metal arc welding*, IOP Conference Series: Materials Science and Engineering, 2018, 400(2), 022027
[36] **Goldak J., Bibby M., Moore J., House R., Patel B.,** *Computer modelling of heat flow in welds*, Metallurgical Transactions B, vol. 17 B, 1986, pp. 587-600.